INTERNATIONAL JOURNAL FOR NUMERICAL METHODS IN FLUIDS
Int. J. Numer. Meth. Fluids **31**: 451–479 (1999)

THREE-DIMENSIONAL LINEAR STABILITY ANALYSIS OF INCOMPRESSIBLE VISCOUS FLOWS USING THE FINITE ELEMENT METHOD

YAN DING* AND MUTSUTO KAWAHARA

Department of Civil Engineering, Chuo University, Kasuga 1-13-27, Bunkyo-ku, Tokyo 112-8551, Japan

SUMMARY

The linear stability of incompressible flows is investigated on the basis of the finite element method. The two-dimensional base flows computed numerically over a range of Reynolds numbers are perturbed with three-dimensional disturbances. The three-dimensionality in the flow associated with the secondary instability is identified precisely. First, by using linear stability theory and normal mode analysis, the partial differential equations governing the evolution of perturbation are derived from the linearized Navier–Stokes equation with slight compressibility. In terms of the mixed finite element discretization, in which six-node quadratic Lagrange triangular elements with quadratic interpolation for velocities (P_2) and three-node linear Lagrange triangular elements for pressure (P_1) are employed, a non-singular generalized eigenproblem is formulated from these equations, whose solution gives the dispersion relation between complex growth rate and wave number. Then, the stabilities of two cases, i.e. the lid-driven cavity flow and flow past a circular cylinder, are examined. These studies determine accurately stability curves to identify the critical Reynolds number and the critical wavelength of the neutral mode by means of the Krylov subspace method and discuss the mechanism of instability. For the cavity flow, the estimated critical results are $Re_c = 920.277 \pm 0.010$ for the Reynolds number and $k_c = 7.40 \pm 0.02$ for the wave number. These results are in good agreement with the observation of Aidun *et al.* and are more accurate than those by the finite difference method. This instability in the cavity is associated with *absolute instability* [Huerre and Monkewitz, *Annu. Rev. Fluid Mech.*, **22**, 473–537 (1990)]. The Taylor–Göertler-like vortices in the cavity are verified by means of the reconstruction of three-dimensional flows. As for the flow past a circular cylinder, the primary instability result shows that the flow has only two-dimensional characteristics at the onset of the von Kármán vortex street, when $Re < 49$. The estimated critical values of primary instability are $Re_c = 46.389 \pm 0.010$ and $St_c = 0.126$ for the Strouhal number. These values are very close to the observation data [Williamson, *J. Fluid Mech.*, **206**, 579–627 (1989)] and other stability results [Morzynski and Thiele, *Z. Agnew. Math. Mech.*, **71**, T424–T428 (1991); Jackson, *J. Fluid Mech.*, **182**, 23–45 (1987)]. This onset of vortex shedding is associated with the symmetry-breaking bifurcation at the Hopf point. Copyright © 1999 John Wiley & Sons, Ltd.

KEY WORDS: hydrodynamic stability; incompressible flow; mixed finite element method; cavity flow; circular cylinder flow

1. INTRODUCTION

The transition of fluid flow is a very complicated phenomenon that can be characterized only by means of many parameters, in which the Reynolds number *Re* is the most important. The

* Correspondence to: Department of Civil Engineering, Chuo University, Kasuga 1-13-27, Bunkyo-ku, Tokyo 112-8551, Japan. E-mail: ding@sip.civil.chuo-u.ac.jp

CCC 0271–2091/99/180451–29$17.50

Received April 1997
Revised April 1998

stability of parallel flows, such as plane Poiseuille flow and boundary layer flows, due to the similarity of velocity profile in streamwise, can be described as a *local* stability governed by the Orr–Sommerfeld equation, which is at least a fourth-order ordinary differential equation. The neutral curve can be identified from the spatial modes or/and temporal modes by means of calculating a generalized eigenproblem. The calculation of these eigenproblems is very complex, even for the simplest canonical flows [2].

Numerical methods have been applied to theoretical studies of instability and transition to turbulence since shortly after the advent of the digital computer. A rationally asymptotic framework was developed for treating the *globally* linear and weakly non-linear stability of non-parallel flows by means of the finite difference [4] and spectral methods [5]. Linear theory is applicable to some transition problems, and it may describe the first stage of transition—the (usually) slow growth of the primary instability. By means of three-dimensional disturbance with primary instability waves, the secondary instability can also be analysed by a variety of numerical methods.

Kleiser and Zang [6] have reviewed the discretization in space and time of the Navier–Stokes equations by using the finite difference method, the spectral method, and/or the spectral domain decomposition method. The precise choice of discretization in space is primarily governed by efficiency and convenience. However, the numerical methods as stated above are limited to quite simple geometries [7–9]. Even for finite difference methods, co-ordinates transformation is necessary in order to simulate simple geometries [10,11]. In contrast, with the finite element method (FEM), complex geometries can be described exactly and effectively. Li and Kot [12], as the earlier researchers, analysed one-dimensional Poiseuille flow using the FEM and Hermitian interpolation. Jackson [13] discussed in detail the onset of vortex shedding in flow past variously shaped bodies using the Newton–Raphson iteration. Kawahara and Ding [14] investigated the generic feature of bifurcation for a brown tide over a natural ocean bay by using the FEM. These studies showed that the FEM has the advantage of effectively obtaining the accurate result of stability analysis.

To determine the stability of an incompressible flow, the principle of linearized stability is required. The linear stability problem can be treated as a generalized eigenproblem, in which the leading eigenvalue with a maximum real part determines the stability of the base flow. By choosing primitive variables (i.e. u/p variables), there are three aspects of numerical technical difficulties associated with this generalized eigenproblem. First, the spectrum of this generalized eigenproblem is singular or defective due to the continuity constraint of incompressible flow. Further detail regarding the eigenstructure for Stokes problem can be found in [15]. For $Re > 0$, the basic structure remains the same with the exception that, because of the unsymmetric matrix, the eigenvalues are complex. Second, with respect to the existence and uniqueness of the solution associated with the solution, independent of finite element size, the chosen finite element subspace should satisfy the *LBB* condition (div–stability or Ladyzhenskaya–Babuska–Brezzi or *inf–sup* condition) [15,16]. An unsuitable choice of element type will lead to the spatial oscillation of pressure, although the dispersion relation of stability cannot be affected significantly [17]. Last, in order to satisfy convergence, accuracy, and high resolution of eigenvectors with steep gradients in complex geometry, a sufficiently large nodal number or fine mesh is needed. Thus, an effective and economical numerical algorithm should be developed to solve the unsymmetric large eigenproblem with finite elemental structure. To this end, the Krylov subspace method [26,27] is employed in the calculation of the eigenproblem contained in the stability problem of incompressible flow in which the linear fractional transformation for spectrum is used.

The purpose of this study is to analyse the linear stabilities of incompressible flows by employing the mixed finite element method. Focus is on the two kinds of flows. The first case is internal flow in a lid-driven cavity. Ramanan and Homsy [4] reviewed cavity flow from experimental and numerical studies. The main conclusion can be summarized as the following observation. It appears that the flow is most definitely two-dimensional when the Reynolds number is less than 500. At some critical Reynolds number below 1000, there is a transition to secondary state. Reliable experimental results have been shown by Aidun *et al.* [1] for this range of Reynolds number. It is shown that the critical Reynolds number in cavity flow is in the range 825–925, has the order $O(10^3)$, the corresponding non-dimensional frequency in the spanwise direction is approximately 0.1, i.e. $O(10^{-1})$. The second case in this paper is the external flow past a circular cylinder whose primary instability of steady state is examined. Abundant literature can be found for the investigation of stability of flow past a circular cylinder [10,11,13,18]. The basic knowledge for the primary instability is that the steady flow with a pair of symmetric recirculation regions behind the cylinder is destabilized when $Re < 49$, the onset of vortex shedding will happen as one increases the Re number. An excellent comprehensive review concerned with the vortex dynamics in the cylinder wake is given by Williamson [18].

For this study, the base flows of lid-driven cavity and circular cylinder are two-dimensional, which are computed by means of an improved velocity correction method by which the constraint of continuity can be satisfied [19]. Then, focus is on the linear stabilities of flows in a lid-driven cavity and past a circular cylinder in which the three-dimensional disturbances are allowed for. The main assumption of this study is that the cavity and cylinder are of infinitely axial extent, which allow for the eigenproblem to be decomposed into normal mode in the spanwise direction. To overcome the singularity of the eigenproblem in the linear analysis of incompressible flows [15], a slight compressibility is further employed to eliminate the singularity. In addition, Khorrami *et al.* [8] stated that the singular effect on the desired (physical) eigenvalues was negligible. In terms of the mixed finite element discretization, in which six-node quadratic Lagrange triangular elements with quadratic interpolation for velocities (P_2) and three-node linear Lagrange triangular elements for pressure (P_1) are employed, the non-singular generalized eigenproblem is formulated from these equations whose solution gives the dispersion relation between complex growth rate and wave number. The stability results obtained from P_2P_1 elements are compared with those from P_1P_1 elements [20] (see Figures 4 and 5). It is shown that, as in the simulation of incompressible flows with the mixed finite element method, the spatial distribution of pressure disturbance can be smoothed by using the P_2P_1 element; however, the choice of element type does not have a significant influence on the stability results. As for the stability of cavity flow, the critical results are $Re_c = 920.277 \pm 0.010$ for the Reynolds number and $k_c = 7.40 \pm 0.02$ for the wave number. These results are much closer to the observation [1] than those from the finite difference method with a three-dimensional potential formulation [4]. In addition, the three-dimensional cavity flow structure is reconstructed by means of normal mode for the critical flow (see Figures 10–12). It shows that the Taylor–Göertler-like vortices in cavity exist in the spanwise direction and are similar to the numerical results [21]. With respect to the instability of flow past a circular cylinder, the obtained critical values of primary instability are $Re_c = 46.389 \pm 0.010$ for Reynolds number and $St_c = 0.126$ for Strouhal number. These results are in good agreement with the experimental data by Williamson [3] and other results by stability analysis [10,13]. The stability analysis shows that the primary instability in the cylinder wake is *intrinsically* two-dimensional.

The remainder of the paper is organized as follows. Section 2 describes the mathematical formulations, including the linearized Navier–Stokes equations with a slight compressibility. In Section 3, the numerical method for the simulation of steady flow and effective eigenspectrum solver are discussed. In Section 4, the numerical results of linear stability are presented for two cases and the reconstructed three-dimensionally critical flow patterns. The instability mechanism for cavity flow and circular cylinder flow is also discussed. Section 5 concludes this paper.

2. MATHEMATICAL FORMULATIONS

There are two different methods to derive the mathematical formulations of the stability analysis for incompressible fluid flows. One is to form a non-singular eigenproblem by defining two potential functions in three-dimensional space [4,15]. Therefore, in general, definite potential functions are adopted to force the velocity field to be solenoidal, and automatically satisfy the continuity equation [22]. But it should be pointed out that with potential formulations, it is plausible to specify boundary conditions for the potential functions. In addition, it will result in a coupled set of fourth-order partial differential equations for the potentials when using the finite difference method reported in [4]. Therefore, if using the finite element discretization, a Hermitian interpolation function is needed for the discretization of those equations, at least it implies that the total degree of freedom would increase by twice the total nodal number. Thus, it is inconvenient and time-consuming to solve this kind of linear algebraic equations derived from the FEM.

Another way is to write the governing equations in primitive variables in order to utilize Lagrangian interpolation functions in finite elemental space. It will keep the linear algebraic system within an appropriate memory size. In this study, the latter method is adopted, i.e. u/p variables, to form a discretized system of the FEM, with slight compressibility so as to eliminate the singularity in the eigenproblem.

2.1. Formulations

Considering three-dimensional flows in a lid-driven cavity and past a circular cylinder that are infinitely long in the spanwise direction, in which the scale of velocity V_0 is defined as the top boundary moving velocity in cavity or the uniform inflow velocity for flow past a circular cylinder. The length scale L is defined as the width or height of the cavity or the diameter of the circular cylinder. Assume that the fluid is slightly compressible, isothermal, and Newtonian. In addition, the non-dimensional scales for time, density, and kinematic pressure are L/V_0, ρ_0 and CV_0, where C is acoustic speed of fluid. The dimensionless form of continuity for a Newtonian fluid flow is

$$\frac{\mathrm{D}\rho}{\mathrm{D}t} + \rho \nabla \cdot \mathbf{v} = 0 \quad \text{in } \Omega, \tag{1}$$

where $\mathrm{D}/\mathrm{D}t$ is mass differentiation with respect to dimensionless time, ρ and $\mathbf{v}$ denote the non-dimensional density and velocity vector respectively. By introducing a slight compressibility, given that pressure is only a function of density, you get

$$\frac{\mathrm{D}p}{\mathrm{D}\rho} = \frac{1}{\rho Ma} \frac{\mathrm{D}\rho}{\mathrm{D}t}, \tag{2}$$

where $Ma = V_0/C$ denotes the Mach number in the fluid. Substituting (2) into (1), the modified continuity equation with a slightly compressible assumption can be written as follows:

$$\frac{\mathrm{D}p}{\mathrm{D}t} + \frac{1}{Ma}\nabla\cdot\mathbf{v} = 0 \quad \text{in } \Omega. \tag{3}$$

To derive the equation of motion, consider the constitutive relation of a Newtonian fluid with Stokes's hypothesis [23], for which the stress tensor $\mathbf{T}$ is

$$\mathbf{T} = -\frac{1}{Ma}p\mathbf{I} + \frac{2}{Re}\left(\mathbf{S} - \frac{1}{3}\mathbf{I}\nabla\cdot\mathbf{v}\right), \tag{4}$$

where $\mathbf{I}$ is the identity matrix, $Re = V_0 L/v$ indicates the Reynolds number in a flow in which v is the kinematic viscosity, and the rate-of-strain tensor $\mathbf{S}$ is

$$\mathbf{S} = \frac{1}{2}[\nabla\mathbf{v} + (\nabla\mathbf{v})^T]. \tag{5}$$

Under the condition of slight compressibility, considering v of fluid a constant and $\mathbf{f}$ a constant body force (e.g. gravitation), the non-dimensional momentum equation can be written as

$$\frac{\mathrm{D}\mathbf{v}}{\mathrm{D}t} = -\frac{1}{Ma}\nabla p + \frac{1}{Re}\left[\nabla^2\mathbf{v} + \frac{1}{3}\nabla(\nabla\cdot\mathbf{v})\right] + \mathbf{f} \quad \text{in } \Omega, \tag{6}$$

provided $\Gamma = \Gamma_N \cup \Gamma_S$, in which Γ_S denotes the Dirichlet boundaries and Γ_N the Neumann boundaries. No-slip conditions are imposed on all wall boundaries. The boundary conditions

$$u = 1 \quad \text{and} \quad v = 0 \quad \text{on } \Gamma_S \tag{7}$$

are specified on the top of the cavity or the uniform inflow of the circular cylinder. The Neumann condition on the top of the cavity or the outflow boundary is

$$\mathbf{T}\cdot\mathbf{n} = \hat{t} \quad \text{on } \Gamma_N, \tag{8}$$

where $\mathbf{n}$ denotes the boundary normal unit vector, and $\hat{t}$ indicates a specified value on the boundary. In practical cases, the value of $\hat{t}$ is set to zero for the two cases considered.

2.2. Base flow

As the cavity or circular cylinder are assumed as infinitely long in the spanwise direction, the base flow whose stability is being examined is two-dimensional and steady, with the result that the equations for this flow simplify to

$$\nabla\cdot\mathbf{V} = 0 \quad \text{in } \Omega, \tag{9}$$

$$\mathbf{V}\cdot\nabla_*\mathbf{V} = -\nabla_* P + \frac{1}{Re}\nabla_*^2\mathbf{V} \quad \text{in } \Omega, \tag{10}$$

where $\mathbf{V}$ and P are the velocity and kinematic pressure in the base flow respectively. ∇_* represents the two-dimensional gradient operator.

2.3. Perturbation equations

To investigate the stability of the base flow to disturbances, equations that govern the evolution of these perturbations are required. To this end, the base flow is perturbed by a disturbance velocity $\mathbf{v}'$ and the kinematic pressure by p'. The total velocity and pressure are then written as

$$\mathbf{v} = \mathbf{V} + \mathbf{v}' \quad \text{and} \quad p = P + p'. \tag{11}$$

Substituting these into the continuity equation (3) and the equation of motion (6), subtracting the base flow equations (9) and (10) and linearizing, the following equations for the perturbation pressure and velocity subject to no-slip conditions on the Dirichlet boundaries are obtained.

p' equation

$$\frac{\mathrm{D}p'}{\mathrm{D}t} + (\mathbf{v}'\cdot\nabla)P + \frac{1}{Ma}\nabla\cdot\mathbf{v}' = 0 \quad \text{in } \Omega, \tag{12}$$

$\mathbf{v}'$ equations

$$\frac{\mathrm{D}\mathbf{v}'}{\mathrm{D}t} + (\mathbf{v}'\cdot\nabla)\mathbf{V} = -\frac{1}{Ma}\nabla p' + \frac{1}{Re}\left[\nabla^2\mathbf{v}' + \frac{1}{3}\nabla(\nabla\cdot\mathbf{v}')\right] \quad \text{in } \Omega, \tag{13}$$

where the two-dimensional operator is

$$\frac{\mathrm{D}}{\mathrm{D}t} = \frac{\partial}{\partial t} + (\mathbf{V}\cdot\nabla_*).$$

The boundary conditions of the disturbances are

$$\mathbf{v}' = 0 \quad \text{on } \Gamma_{\mathrm{S}}, \tag{14}$$

$$\left(-\frac{1}{Ma}p'\mathbf{I} + \frac{2}{Re}\left(\mathbf{S}' - \frac{1}{3}\mathbf{I}\nabla\cdot\mathbf{v}'\right)\right)\cdot\mathbf{n} = 0 \quad \text{on } \Gamma_{\mathrm{N}}, \tag{15}$$

where $\mathbf{S}' = \frac{1}{2}[\nabla\mathbf{v}' + (\nabla\mathbf{v}')^T]$. In terms of the normal mode, the disturbances of pressure and velocities in the symmetry plane and spanwise direction of flow are presented as

$$p' = i\hat{p}(x, y)\exp(i\kappa z + \omega t), \tag{16}$$

$$u' = i\hat{u}(x, y)\exp(i\kappa z + \omega t), \tag{17}$$

$$v' = i\hat{v}(x, y)\exp(i\kappa z + \omega t), \tag{18}$$

$$w' = \hat{w}(x, y)\exp(i\kappa z + \omega t) \tag{19}$$

respectively, where i is the imaginary unit, κ is the spanwise wave number and $\omega = \omega_{\mathrm{r}} + i\omega_{\mathrm{i}}$ denotes the complex growth rate. One of the reasons for the choice of the imaginary amplitude in normal modes is to avoid complex arithmetic in the following calculation of the eigenproblem. The assumed form of the eigenvector is completely general and allows for both steady and oscillatory modes, depending on whether the eigenvalue ω is real or complex respectively. According to linear stability theory, if ω is real, the disturbances either grow or decay monotonically, the critical Reynolds number is that for which $\omega = 0$. If ω is complex, the neutral condition is $\omega_{\mathrm{r}} = 0$, and the onset of instability is oscillatory with dimensionless wave speed ω_{i}. This normal mode form also includes time-dependent two-dimensional instability of the steady flow for which $\kappa = 0$. Substituting these normal modes into (12) and (13), one can present an eigenproblem with the growth rate being the eigenvalue

$$\omega\hat{p} + (\mathbf{V}\cdot\nabla_*)\hat{p} + (\hat{\mathbf{v}}\cdot\nabla_*)P + Ma^{-1}(\nabla_*\cdot\hat{\mathbf{v}} + \kappa\hat{w}) = 0, \tag{20}$$

$$\omega\hat{u} + (\mathbf{V}\cdot\nabla_*)\hat{u} + (\mathbf{v}\cdot\nabla_*)U + Ma^{-1}\frac{\partial\hat{p}}{\partial x} = Re^{-1}\left[(\nabla_*^2 - \kappa^2)\hat{u} + \frac{1}{3}\frac{\partial}{\partial x}(\nabla_*\cdot\hat{\mathbf{v}} + \kappa\hat{w})\right], \tag{21}$$

$$\omega\hat{v} + (\mathbf{V}\cdot\nabla_*)\hat{v} + (\hat{\mathbf{v}}\cdot\nabla_*)V + Ma^{-1}\frac{\partial\hat{p}}{\partial y} = Re^{-1}\left[(\nabla_*^2 - \kappa^2)\hat{v} + \frac{1}{3}\frac{\partial}{\partial y}(\nabla_*\cdot\hat{\mathbf{v}} + \kappa\hat{w})\right], \tag{22}$$

$$\omega\hat{w} + (\mathbf{V}\cdot\nabla_*)\hat{w} - Ma^{-1}\kappa\hat{p} = Re^{-1}\left[(\nabla_*^2 - \kappa^2)\hat{w} - \frac{1}{3}\kappa(\nabla_*\cdot\hat{\mathbf{v}} + \kappa\hat{w})\right], \tag{23}$$

subject to the no-slip boundary conditions

$$\hat{u} = \hat{v} = \hat{w} = 0 \quad \text{on } \Gamma_S, \tag{24}$$

the stress condition for $\hat{u}$ and $\hat{v}$ is

$$\left(-\frac{1}{Ma}\hat{p}\mathbf{I}^* + \frac{1}{Re}\left(\nabla\hat{\mathbf{v}} + \frac{1}{3}\mathbf{I}^*(\nabla_*\cdot\hat{\mathbf{v}} + \kappa\hat{w})\right)\right)\cdot\mathbf{n} = 0 \quad \text{on } \Gamma_N, \tag{25}$$

where $\mathbf{I}^*$ denotes the two-dimensional identity matrix, and the Neumann condition for $\hat{w}$ is

$$\nabla\hat{w}\cdot\mathbf{n} = 0 \quad \text{on } \Gamma. \tag{26}$$

Thus, the boundary conditions are consistent with those in the simulation of base flows. Meanwhile, Equations (20)–(23) can be rewritten in the compact form, i.e.

$$\omega\hat{\phi} = \mathscr{L}(\mathbf{V}, P, \kappa)\hat{\phi}, \tag{27}$$

where $\hat{\phi} = \{\hat{u}, \hat{v}, \hat{w}, \hat{p}\}^T$, $\mathscr{L}$ is the linear operator including the convection, pressure gradient, viscosity and compressibility terms. Because the eigenvector $\hat{\phi}$ depends on the two-dimensional space, the full three-dimensional stability problem at any fixed Re number can be reduced to a one-parameter family of two-dimensional stability problems.

2.4. Finite element formulations

As for the discretization of (20)–(23) by means of the mixed finite element method, the mixed interpolations for velocity and pressure eigenfunctions can be expressed as

$$\hat{\mathbf{v}} = \Phi_\alpha\hat{\mathbf{v}}_\alpha \quad (\alpha = 1, 2, \ldots, 6),$$
$$\hat{p} = \Psi_\lambda\hat{p}_\lambda \quad (\lambda = 1, 2, 3),$$

where Φ_α is the quadratic interpolation function for velocities in a six-node triangular element, Ψ_λ is the linear interpolation for pressure in a three-node triangular element, and $\hat{\mathbf{v}}_\alpha$ and $\hat{p}_\lambda$ represent the nodal values at the αth node of the finite elements. The corresponding weighting functions are similar to the above. After the superposition of the element matrices, the temporal mode of stability is expressed as the generalized eigenproblem in the following form:

$$\mathbf{A}\boldsymbol{\Phi} = \omega\mathbf{B}\boldsymbol{\Phi}, \tag{28}$$

where $\mathbf{A}$, $\mathbf{B}$ and $\boldsymbol{\Phi}$ denote the discretized matrix of the linear operator $\mathscr{L}$, the assembling consistent mass matrix and the discretized eigenfunction $\hat{\phi}$ respectively. If N is the number of total nodal points, and N_b is the total degrees of freedom on all no-slip boundaries for perturbed velocities. The dimensions of the square matrices $\mathbf{A}$ and $\mathbf{B}$ can be reduced to $3(N - N_b)$ through column operations. It follows that the ranks of $\mathbf{A}$ and $\mathbf{B}$ are $3(N - N_b)$. Furthermore, by employing Arnoldi's method [26,27] as the spectrum solver, it is unnecessary to execute the column operation for matrices $\mathbf{A}$ and $\mathbf{B}$, as only linear algebraic equations are needed when solving by means of this kind of subspace iteration method. The Neumann

conditions for perturbation pressure are included implicitly in the finite elemental eigenvalue equation (28).

3. NUMERICAL METHODS

In this section, the numerical methods are described to compute the base flows in a cavity and past a circular cylinder and solve the corresponding eigenproblems for the identification of the critical state flows.

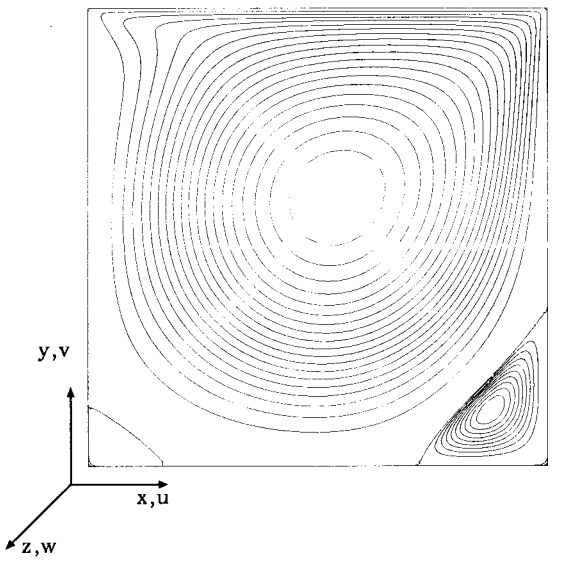

(a)

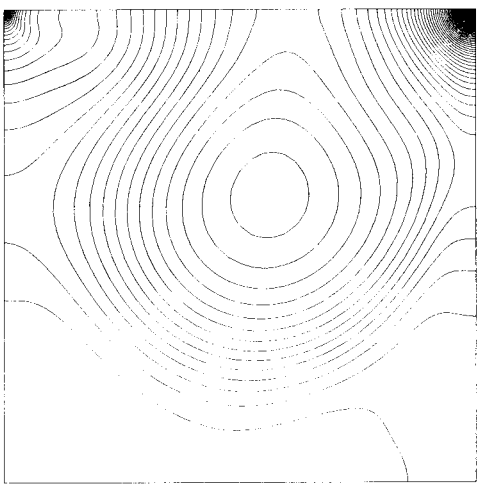

(b)

Figure 1. Two-dimensional steady flow in lid-driven cavity at $Re = 900$. (a) Streamlines (streamfunctions $\psi_{max} = 1.080 \times 10^{-3}$, $\psi_{min} = -0.116$); (b) isobars ($P_{max} = 0.717$, $P_{min} = -0.120$).

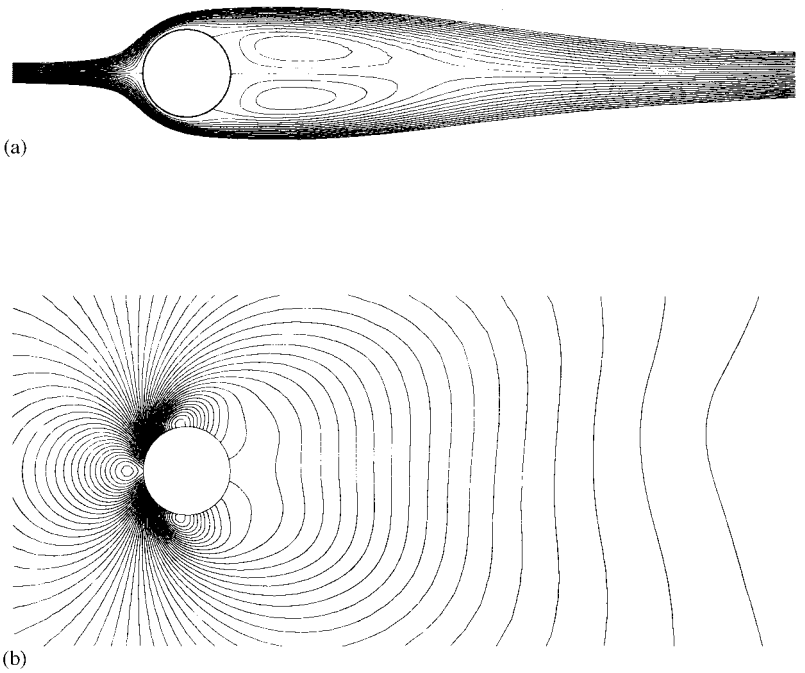

Figure 2. Two-dimensional steady flow past a circular cylinder at $Re = 40$. (a) Streamlines; (b) isobars ($P_{max} = 0.278$, $P_{min} = -0.366$).

3.1. Base flow simulation

The evaluation of the two-dimensional base flows are performed by using the improved velocity correction method with constraint of continuity by means of the FEM [19]. These kinds of methods, based on the fractional step scheme, have been investigated widely, see Kim and Moin [21] for the finite difference method, Jiang and Kawahara [24] and Hawken *et al.* [25] for the FEM. The results from various numerical methods for simulation of two-dimensional cavity flow and flow past a circular cylinder have good accuracy in comparison with experimental data for lower or moderate Re numbers. After the convergence tests for the grid size, it was found that for cavity flow, at the lower Reynolds numbers (i.e. below $Re = 300$) a 33×33 grid is adequate for obtaining grid invariant results, but for the higher Reynolds numbers, the finer 81×81 mesh is necessary. For the flow past a circular cylinder, a fine mesh with 9870 nodal points and 12800 triangular elements for velocities was used to obtain a grid-independent result at $Re < 50$. Details of the solution methodology on a related problem have been reported elsewhere [19]. Figure 1 shows the two-dimensional flow structure in cavity at $Re = 900$, which consists of a primary vortex, secondary vortices at the bottom corners, and an incipient vortex in the upper left-hand corner in Figure 1(a). The steady distribution of pressure at this Reynolds number is shown in Figure 1(b). Figure 2 represents the steady flow past a circular cylinder at $Re = 40$ in which symmetric recirculations exist behind the cylinder.

3.2. Solution of eigenproblem

In the generalized eigenproblem (28), the eigenvalue set of the real unsymmetric matrix contains real values and complex conjugate pairs. To detect the onset of instability, one needs

to identify those that possess eigenvalues closest to the imaginary axis. The leading or dominant eigenvalue that is sought is that with the maximum real part. In this section, a linear fractional transformation (LFT) is discussed briefly within the Arnoldi method. One can find that by means of the purified Arnoldi method, only the eigenvalues with a large module can be obtained [26,27]. In order to search for the dominant eigenvalues with a large real part, in which at least the leading eigenvalue with a maximum real part is involved, it is necessary and convenient to use some simple eigenspectrum transformation technique to transform the spectrum into the desired one [28]. In this study, an LFT is applied to the generalized eigenproblem (28), i.e.

$$\omega = \frac{\tau - 1}{\tau + 1}, \tag{29}$$

which maps the ω spectrum into a τ spectrum in which the eigenvalues of ω are transformed into a unit circle. For the ill-conditioned eigenproblem (28), if the real part of the eigenvalue is finite, the following mapping of spectra exists,

$$\begin{array}{ccc} (\omega_r, \omega_i) & \Leftrightarrow & (\tau_r, \tau_i) \\ (\omega_r, +\infty) & & (-1, 0^+) \\ (\omega_r, -\infty) & & (-1, 0^-) \\ (0^-, \omega_i) & & \left(\dfrac{2}{1+\omega_i^2} - 1, \dfrac{2\omega_i}{1+\omega_i^2}\right) \end{array}.$$

It follows that if ω_i is not so large, the leading eigenvalue $(0^-, \omega_i)$ will be transformed into the right-half plane of the τ spectrum close to the unit circle. Thus, it becomes convenient for Arnoldi's method to detect the dominant set of eigenvalues.

From the LFT, a transformed eigenproblem of (28) is obtained in which the outer part of the τ spectrum is desirable, i.e.

$$-(\mathbf{A} + \mathbf{B})\Phi = \tau(\mathbf{A} - \mathbf{B})\Phi. \tag{30}$$

To apply it to the standard Arnoldi's method, considering the following equivalent relation, i.e.

$$(\mathbf{A} - \mathbf{B})^{-1}(\mathbf{A} + \mathbf{B}) \equiv \mathbf{I} + 2(\mathbf{A} - \mathbf{B})^{-1}\mathbf{B}, \tag{31}$$

where $\mathbf{I}$ is the identity matrix, only the following linear algebraic equations need to be solved

$$(\mathbf{A} - \mathbf{B})w_j = \mathbf{B}v_j. \tag{32}$$

So an LU decomposition of $(\mathbf{A} - \mathbf{B})$ with partial pivoting once in the Arnoldi iteration can be performed, and solve it by back substitution. For further discussion about the incomplete LU factorization, see Elman [29,30]. He showed that the stabilized methods for non-self-adjoint matrix is much more robust than standard incomplete factorizations. The detailed performance of this transformation was discussed by Ding and Kawahara [17].

4. NUMERICAL RESULTS

In this section, the results for the lid-driven cavity flow and the flow past a circular cylinder are presented. As mentioned above, the base flows were computed as a discrete sequence and

used for stability analysis. Since the computed fluid is water, in the computation of eigenproblem, this fluid was considered with a physical compressibility in which the acoustic speed was chosen as 1449.35 $m\,s^{-1}$ in correspondence with the general situation of the fluid at temperature 10.0°C. Therefore, the range of Mach numbers is from 4.5×10^{-7} to 1.4×10^{-5}. It means that the slightly compressible assumption is based on physical characteristics in these cases, rather than on the choice of an artificial compressible parameter, such as that in [7,8].

4.1. Case 1—cavity flow for $Re = 0 \sim 1050$

4.1.1. Convergence tests. The correctness of the eigenspectrum obtained from Arnoldi's method by employing a P_1P_1 element has been investigated in [31]. It was found that if one specifies the criterion of convergence, such as the residual norm is less than 10^{-10} and only the

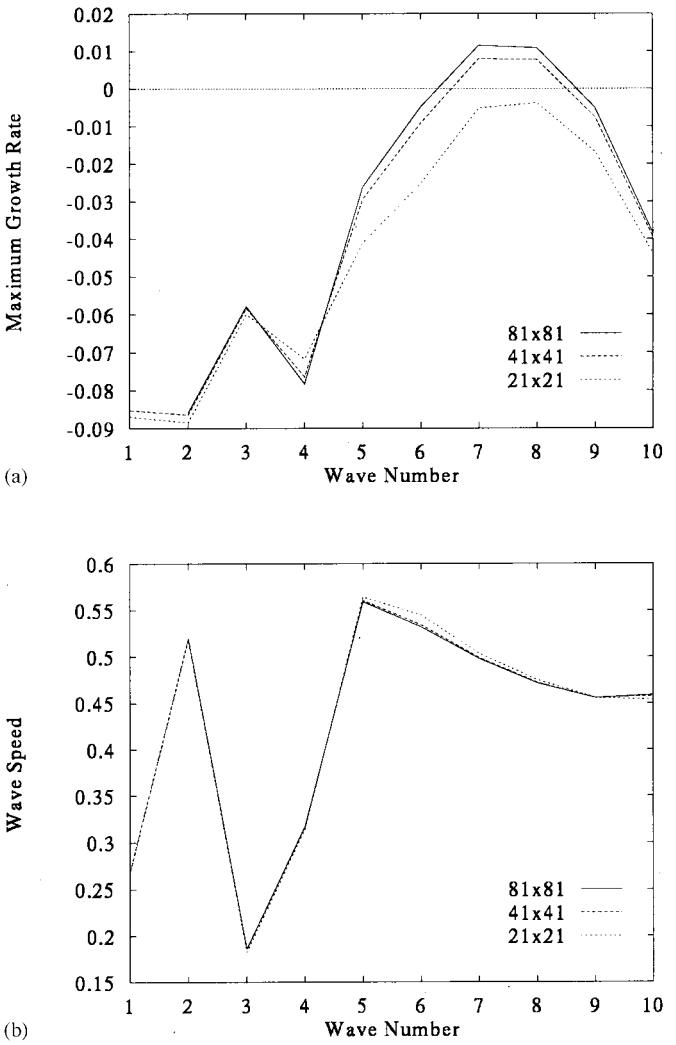

Figure 3. Convergence test for three kinds of meshes (i.e. 21×21, 41×41 and 81×81) (a) Maximum growth rate; (b) wave speed.

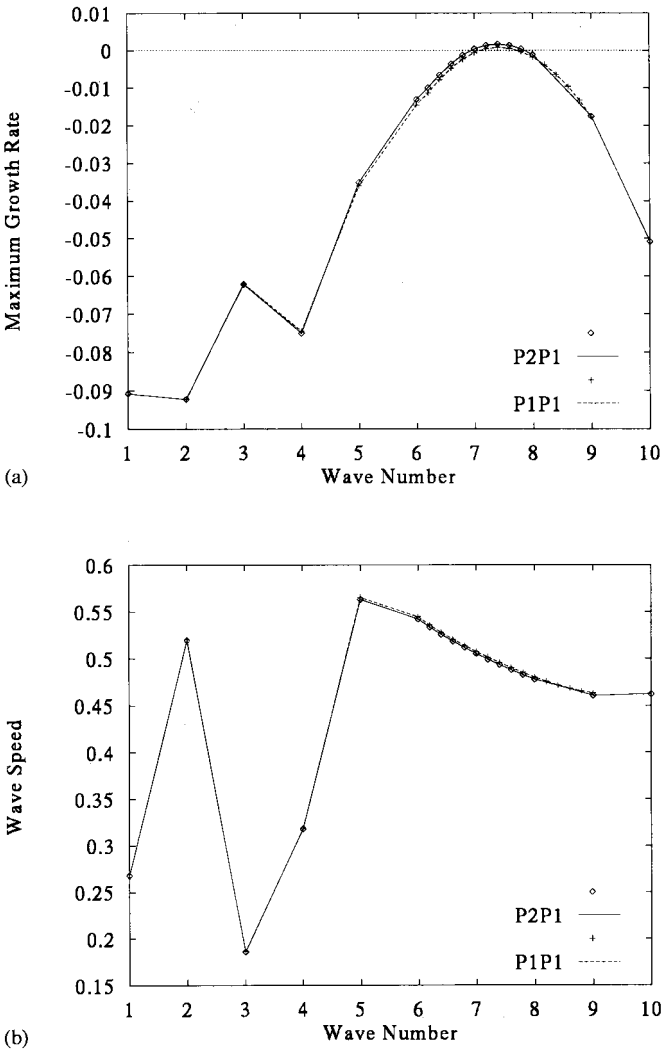

Figure 4. Comparison of stability results from P_2P_1 and P_1P_1 elements for $Re = 930$. (a) Maximum growth rate; (b) wave speed.

first three dominant eigenvalues are needed, the adequate number of Arnoldi's iteration m will be no more than 30. In order to obtain a more accurate eigenspectrum, the value of m is chosen as 60 in all cases of the following computation.

To search for the grid-convergent eigenspectrum for calculation of eigenvalues, due to the memory limitation at computer, grid convergence tests on non-uniform grids (21×21, 41×41 and 81×81) were performed on the basis of P_1P_1 elements. Figure 3 represents the comparison of the dispersion relation for $Re = 1000$ by employing the three kinds of meshes described above. It was found that the grid size has an important impact on the convergence of maximum growth rate (i.e. maximum real part) in Figure 3(a), but little influence on the wave speed (i.e. the imaginary part of the leading eigenvalue) in Figure 3(b). It follows that the convergent eigenvalues are obtained by increasing the grid size. In order to find an accurate

eigensolution, a non-uniform mesh (81×81) is chosen in the following stability analysis of cavity flows.

Further, the results from the P_2P_1 and P_1P_1 elements are compared in Figure 4 for the maximum growth rate (a) and the corresponding wave speed (b), in which an 81×81 mesh is used for velocities and the marks represent the numerically computational points. Figure 4 shows that for unstable flow ($Re = 930$) near the critical flow, the dispersion relation curves are very close to that obtained in the equal-order interpolation method. Also investigated were lower and higher Reynolds numbers, and it was found that the difference between the two elements was negligible.

Next, the distribution of the pressure eigenvector is compared in Figure 5. This figure shows the real eigenvectors of pressure associated with the leading eigenvalue for $Re = 600$ with

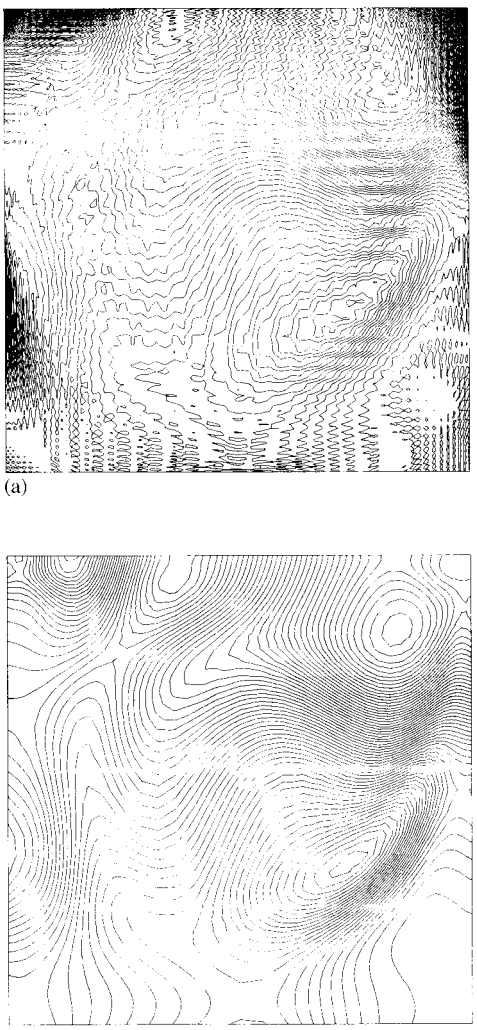

Figure 5. Distribution of real pressure eigenvectors from two kinds of elements for $Re = 600$ with $\kappa = 6$. (a) P_1P_1; (b) P_2P_1.

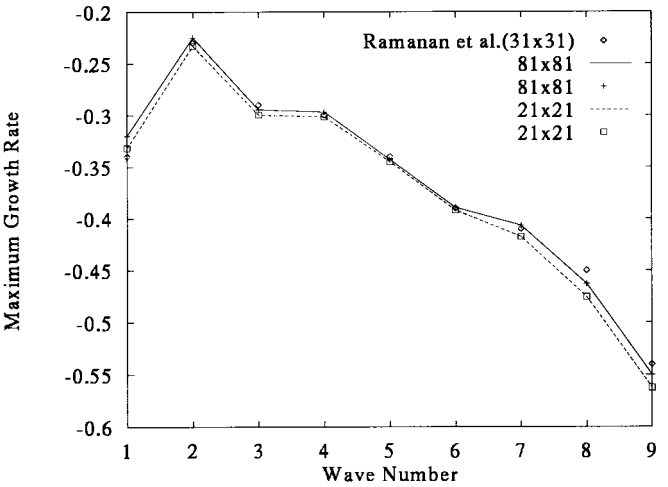

Figure 6. Comparison of real part vs. wave number for $Re = 200$.

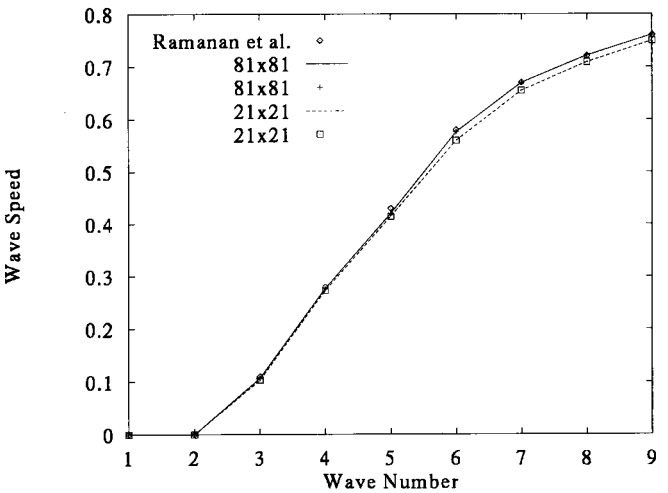

Figure 7. Comparison of imaginary part vs. wave number for $Re = 200$.

$\kappa = 6$. The spatial oscillation of pressure is very pronounced for the result with P_1P_1 elements (Figure 5(a)), however, the mixed finite element with P_2P_1 element remedies the 'wig-waging' distribution of pressure to be the same as for the situation in the simulation of incompressible flow with the mixed finite element method. Therefore, it can be concluded that, for both P_1P_1 and P_2P_1 elements, a convergent eigenspectrum can be obtained, and with the mixed finite element method, the spatial distribution of pressure eigenvector can be smooth. This is the reason that the feature of P_1P_1 element does not satisfy the LBB condition, and attention to the LBB condition should be paid in the calculation of the eigenproblem [16].

4.1.2. Validation of stability results. In order to validate the stability result, the present results by employing meshes 21×21 and 81×81 are compared with those of Ramanan and Homsy [4] in which a 31×31 grid with nine point stencil was employed by means of the finite

difference method, and the spectra of cavity flows were determined by means of the simultaneous iteration method [32]. The comparison of maximum real and corresponding imaginary parts for $Re = 200$ is shown in Figures 6 and 7, respectively. It indicates that the stability curves from the FEM are very close to that obtained with the finite difference method at the lower Reynolds number. It can be seen that the stability results using slight compressibility have good accuracy despite the coarse 21×21 grids. However, the non-uniform mesh 81×81 is employed in the following section in order to sustain the high resolution of eigenspectrum in cavity flow. It was found that the agreement between the two numerically discrete methods only happens over the range of lower Reynolds number (below $Re = 400$). The significant difference between the two methods occurs at high Reynolds numbers. This difference at the critical flow will be presented in the following section.

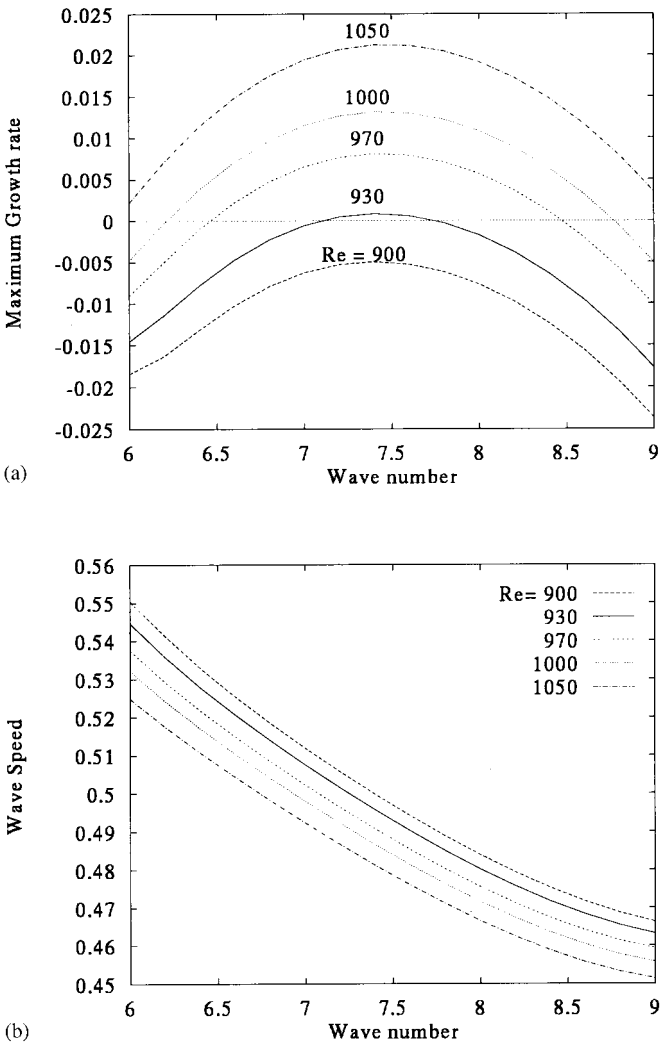

Figure 8. Growth rate wave speed vs. wave number for Reynolds numbers close to critical state. (a) Maximum growth rate; (b) wave speed.

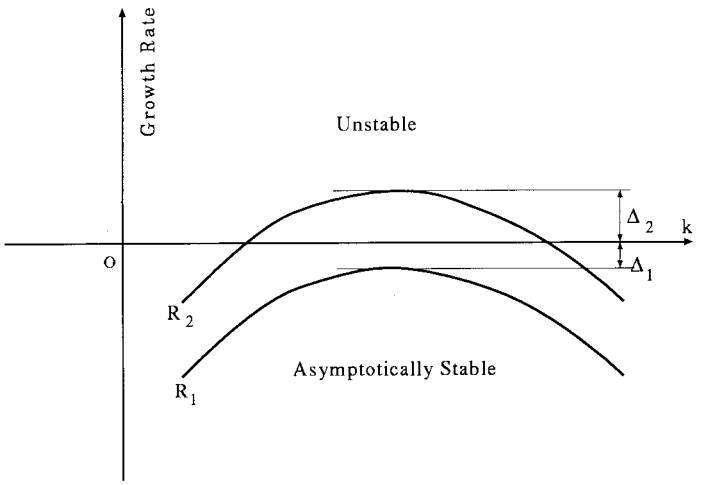

Figure 9. Illustration of dispersion relation in complex plane.

Table I. Iterative procedure of Re_c for cavity flow

n	R_1	Δ_1	R_2	Δ_2	Re_c	$\lvert\Delta R\rvert$	k
1	920.0000	9.65320×10^{-5}	930.0000	1.70859×10^{-3}	920.5348	0.5348	7.4 ± 0.2
2	920.0000	9.65320×10^{-5}	920.5348	7.52795×10^{-5}	920.3005	0.2343	7.4 ± 0.2
3	920.0000	9.65320×10^{-5}	920.3005	1.81862×10^{-5}	920.2529	0.0476	7.4 ± 0.05
4	920.2529	3.87112×10^{-6}	920.3005	1.81862×10^{-5}	920.2513	0.0084	7.40 ± 0.05
5	920.2613	1.87770×10^{-6}	920.3005	1.81862×10^{-5}	920.2650	0.0037	7.40 ± 0.05
5	920.2650	7.53774×10^{-7}	920.3005	1.81862×10^{-5}	920.2664	0.0014	7.40 ± 0.02
6			920.2770	3.28154×10^{-6}	920.2770	0.0106	7.40 ± 0.02

Figure 8 shows the principal results $\omega_r(\kappa, Re)$ for the maximum real parts (growth rate) and the corresponding imaginary part (wave speed) of the leading eigenvalue. Over the range of Reynolds numbers close to the critical state, the discrete increment of wave number $\Delta\kappa$ is as small as 0.2. Therefore, the smooth dispersion relation curve close to the critical flow can be drawn. The growth rate in Figure 8 shows that the critical situation belongs to the Hopf mode, which is very close to $Re = 930$ with $\kappa = 7.5$. It is indicated that the $\kappa = 7.5$ mode crosses the imaginary axis first followed sequentially by the $\kappa = 7$ mode at a slightly higher Reynolds number. It was not found that the lower wave number mode (stationary) crosses the imaginary axis in the discrete sequence of these cavity flows as reported in [4].

4.1.3. Detection of critical Reynolds number Re_c. To detect exactly the critical Reynolds number, the general iterative methodology with linear interpolation is proposed. It is assumed that: if the critical flow with the real part $\omega_r = 0$ exists, find a subcritical flow with the Reynolds number R_1 and a supercritical flow with R_2 close to the real axis in a complex plane as illustrated in Figure 9 for $R_2 > R_1$, seek the $(n+1)$th approximated critical Reynolds number Re_c by means of the following linear interpolation, i.e.

$$R_C^{n+1} \doteq \frac{\Delta_1^n R_2^n + \Delta_2^n R_1^n}{\Delta_1^n + \Delta_2^n}. \tag{33}$$

The iteration procedure for the detection of the critical Reynolds number is shown in Table I. The critical parameters including the leading eigenvalue ω_c, the critical wave number κ_c, and the non-dimensional frequency f_c are listed in Table II. For both P_2P_1 and P_1P_1 elements, the results are very close to each other. However, the Re_c from P_1P_1 is close to the upper critical Reynolds number, but that from P_2P_1 is approximate to the average value of Re_c in the observation [1]. Under the meaning of average, it can be said that the result from P_2P_1 element is more accurate than that from P_1P_1 element. In addition, the results from the FEM are much closer to observation than those from the finite difference method [4], in which the short wavelength mode (Hopf mode with $\kappa = 6$) at a Re close to 700 was reported. From Table II, the critical wavelength is 0.898 close to unit cavity width. The present result can also be compared with the numerical one in [21]. The same conclusion as described above can be shown.

4.1.4. Reconstruction of three-dimensional flow. In order to reproduce the three-dimensional flow field that corresponds to the critical mode, the total three-dimensional flow field is reconstructed on the basis of the two-dimensional steady flow with an arbitrary number of the disturbance eigenvectors. If considering the conjugate pairs of eigenspectrum, the real three-dimensional flows are reconstructed by means of the following superposition of eigenvectors (the general vector of pressure and velocity v are the same as that of u)

$$u = U - 2 \sum_{n=1}^{N_t} \exp(\omega_r^n t \cos(\kappa z)[\hat{u}_i^n \cos(\omega_i^n t) + \hat{u}_r^n \sin(\omega_i^n t)]), \tag{34}$$

$$w = 2 \sum_{n=1}^{N_t} \exp(\omega_r^n t \cos(\kappa z)[\hat{w}_r^n \cos(\omega_i^n t) - \hat{w}_i^n \sin(\omega_i^n t)]), \tag{35}$$

where the subscripts r and i denote the real and imaginary parts of eigenvalue or eigenvector respectively. By introducing four pairs of eigenvectors in the critical mode, including the

Table II. Critical parameters of cavity flow

Element	Re_c	ω_c	κ_c	f_c
P_2P_1	920.2770 ± 0.0100	$3.2815 \times 10^{-6} \pm i4.9525 \times 10^{-1}$	7.40 ± 0.02	0.0788
P_1P_1	925.9249 ± 0.0005	$1.3679 \times 10^{-7} \pm i4.9570 \times 10^{-1}$	7.40 ± 0.05	0.0789
Observation [1]	$825 \sim 925$			$\cong 0.10$

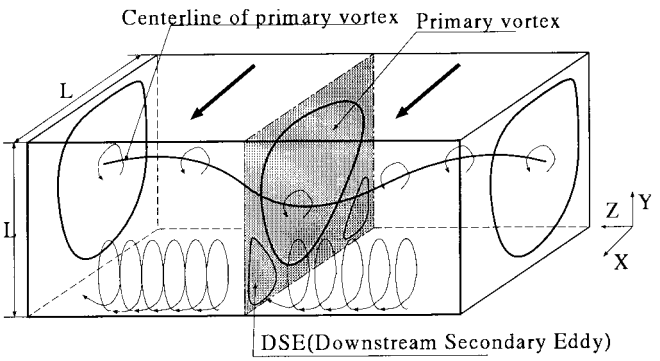

Figure 10. A schematic demonstration of the time periodic vortex for three-dimensional cavity flow.

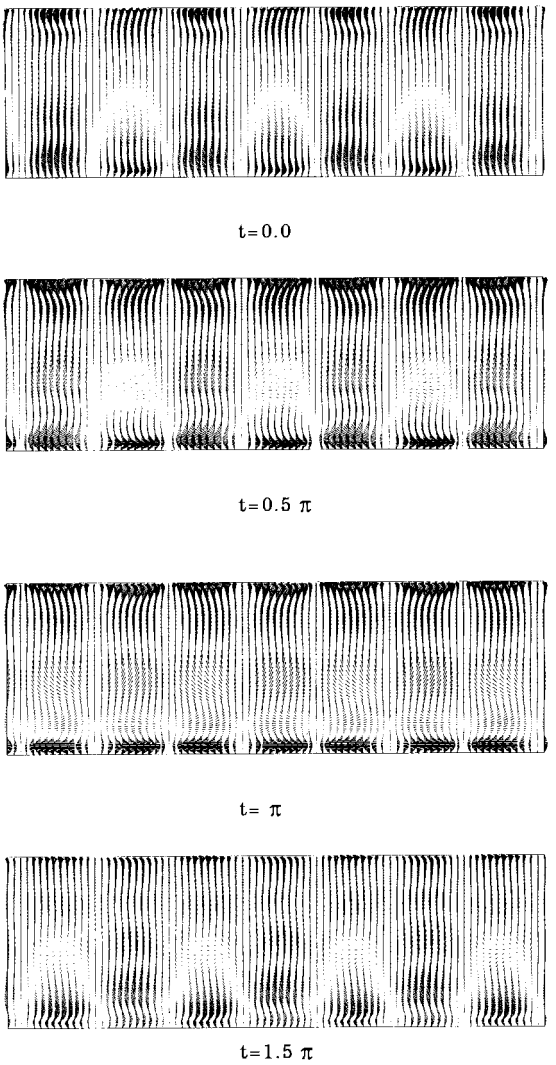

Figure 11. Evolution of velocity fields on y–z plane at $x = L/2$ for Re_c with κ_c; $w_{max} = 3.073 \times 10^{-2}$, $w_{min} = -3.279 \times 10^{-2}$; $v_{max} = 3.499 \times 10^{-2}$, $v_{min} = -2.220 \times 10^{-2}$.

leading pair, the description on the reconstructed flow pattern is summed up, a schematic diagram of this three-dimensional structure is depicted in Figure 10. It appears that in the temporal mode, spiral-shaped vortices superimpose on the primary and the downstream second eddies (DSE) travelling from the symmetry plane outward in the spanwise direction. The disturbance structure near the critical mode is more visible on the DSE rather than the primary vortex. The motion of these vortices is similar to the rotation of a spring around its axis. These results have been proved in the experiment of Aidun *et al.* [1].

To verify the existence of Taylor–Göertler-like vortices (TGL) in the spanwise plane, which were described frequently in the numerically simulation [21,33,34] and experiment of Aidun *et al.* [1], we present the development of the spanwise velocity fields at the symmetry plane for the critical mode in Figure 11. The spanwise fields consist of mushroom-like structures travelling from the symmetry plane outward in the spanwise direction. Due to the maximum order of the

spanwise velocity close to $O(10^{-2})$, TGL vortices in cavity flow are very weak. Similar structures were shown in those observed in flow visualization of Aidun *et al.* [1]. It is easy to show that a cellular structure has a dimensionless wavelength of $\pi/4$ (Kim and Moin [21] showed numerically two pairs of TGL vortices per cavity width at $Re = 1000$). As the ordered cellular structure is crumbled, the transient to turbulence in cavity flow occurs. The contours of the normal vorticity ω_x in the spanwise are represented temporally in Figure 12. The result of ω_x shows that the spanwise motion of the vortex is very weak in the critical flow.

4.2. Case 2—flow past a circular cylinder for $Re < 50$

The aim of this case is to quantify a primary step in the sequence of instabilities leading to turbulence in the wake of a circular cylinder. Specifically, results from a global stability

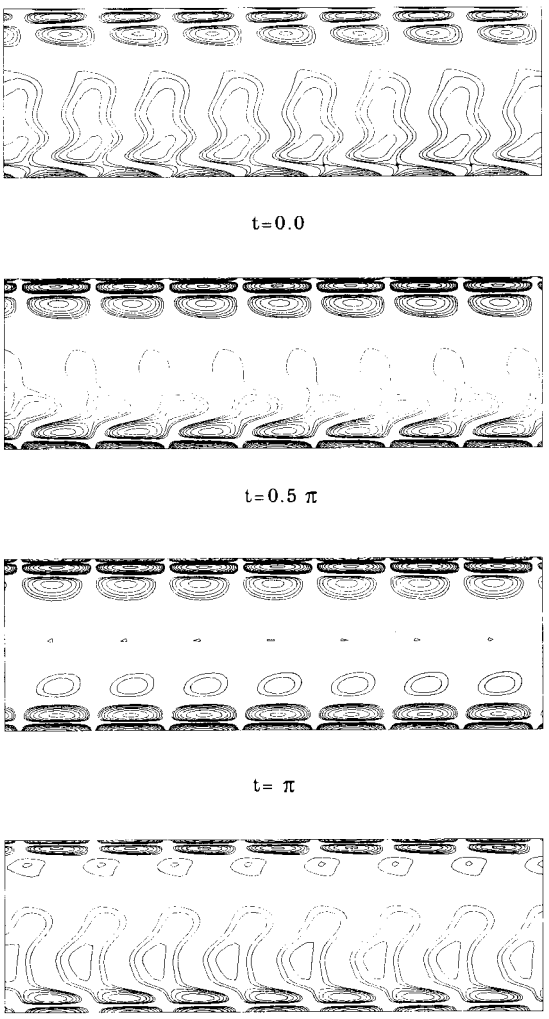

Figure 12. Evolution of normal vorticity ω_x on y–z plane at $x = L/2$ for Re_c with κ_c; ($\omega_{x_{min}} = -1.080$, $\omega_{x_{max}} = 1.082$).

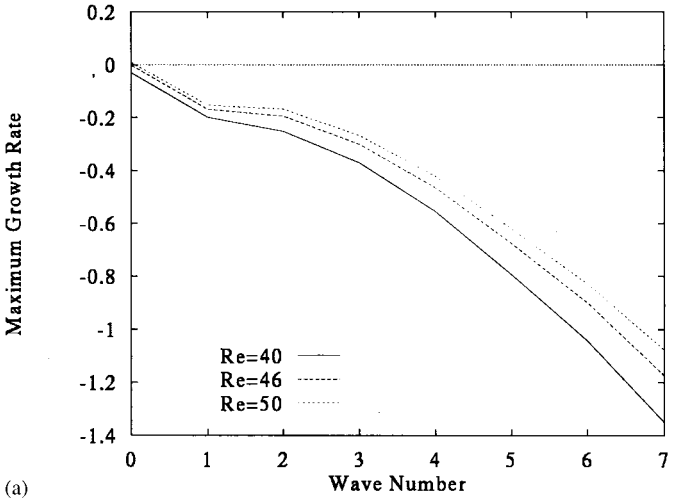

(a)

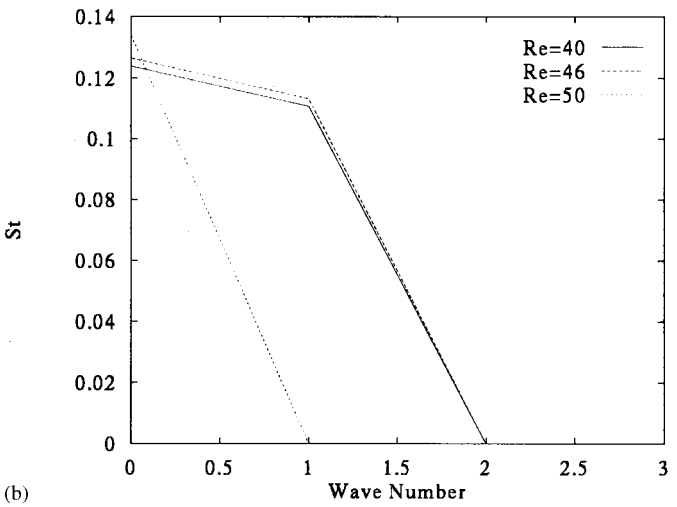

(b)

Figure 13. Dispersion relation of flows past a circular cylinder. (a) Maximum growth rate; (b) wave speed.

analysis of two-dimensional steady flows as described above are presented and the primarily linear instability leading to the von Kármán vortex street is identified precisely. The flow considered is an infinitely long circular cylinder placed perpendicular to an otherwise uniform open flow. The sole parameter, i.e. *Re* number, is defined on the basis of the free-stream velocity V_0 and the cylinder diameter L. For the shedding frequency f, the non-dimensional parameter, i.e. the Strouhal number St, is defined as

$$St \equiv \frac{fL}{V_0} \equiv \frac{\omega_i}{2\pi}, \tag{36}$$

where ω_i is the imaginary part of the leading Hopf mode in the generalized eigenspectrum.

4.2.1. Dispersion relations. The base flows as shown in Figure 2 are perturbed with three-dimensional disturbances, the principal results of $\omega_r(\kappa, Re)$ and the corresponding Strouhal number versus wave number for different Re are depicted in Figure 13(a) and (b). Apparently, the primary instability occurs near $Re \cong 46$, and the onset of vortex shedding for the primary instability is two-dimensional in which the wave number κ near the critical state is equal to zero. This kind of two-dimensionality was reported in Williamson's review [18] and other stability results [10,13].

4.2.2. Detection of Hopf bifurcation point. To determine precisely the critical parameters of the primary instability for flow past a circular cylinder, the linearly iterative calculation as described in Section 4.1.3 was carried out. The iteration procedure for the detection of the critical flow is shown in Table III. After five iterations, the absolute error $|\Delta R|$ of Re_c can be limited to no more than 0.01, the exact critical parameters, i.e. the critical Reynolds number Re_c and Strouhal number St_c, are obtained. The critical eigenmode obtained is a Hopf one as its maximum growth rate is very close to zero (actually, at the real Hopf bifurcation point, the eigenproblem is singular, so only an approximate numerical point can be detected [4,13]).

The comparison of the critical parameters with experimental data [3,35], time-dependent simulation [36], and other linear stability analysis results [10,13] are shown in Table IV. The present result of the critical state, i.e. $Re_c = 46.389 \pm 0.010$ and $St_c = 0.126$, is in good agreement with other results of this critical flow past a circular cylinder [10,13]. The maximum growth rate versus Re is presented in Figure 14(a). In particular, for the critical St_c, convergence tests have been carried out versus Re in Figure 14(a), and the accurate St_c could be obtained at Arnoldi's iteration number $m = 150$, for which the residual norm ε was 1.0×10^{-15} (see Table V). However, the approximated real part of the leading eigenvalue has almost three digits of accuracy, and the St_c has almost five digits of accuracy at $m = 60$. This means that the convergent eigenvalue could be detected when the iteration number m is no more than 60 for the primary instability of the circular cylinder flow. Further, the comparison

Table III. Iterative procedure of Re_c for flows past a circular cylinder

n	R_1	Δ_1	R_2	Δ_2	Re_c	$\lvert\Delta R\rvert$	k
1	46.0000	1.98528×10^{-3}	50.0000	8.39302×10^{-3}	46.7652		0.0
2	46.0000	1.98538×10^{-4}	46.7652	1.91946×10^{-3}	46.3891	0.3761	0.0
3	46.3891	1.97295×10^{-4}	46.7652	1.91946×10^{-3}	46.4242	0.0351	0.0
4	46.3891	1.97295×10^{-4}	46.4242	2.87781×10^{-4}	46.4034	0.0208	0.0
5	46.3891	1.97295×10^{-4}	46.4034	2.80503×10^{-4}	46.3953	0.0090	0.0

Table IV. Comparison of critical parameters

Literature	Re_c	St_c	κ_c	Method	Grid size
Jackson [13]	45.403	0.13626	0.0	FEM with Newton–Raphson method	3056
Morzynski [10]	46.270	0.13451	0.0	FDM with Newton–Raphson method	3200
Williamson [3]	47.90	0.1220		Experiment	
Berger [35]	50.00	0.12		Experiment	
Gresho [36]	50.00	0.14		Two-dimensional simulation by FEM	1852
This paper	46.389	0.12619	0.0	FEM with Arnoldi's method	9870

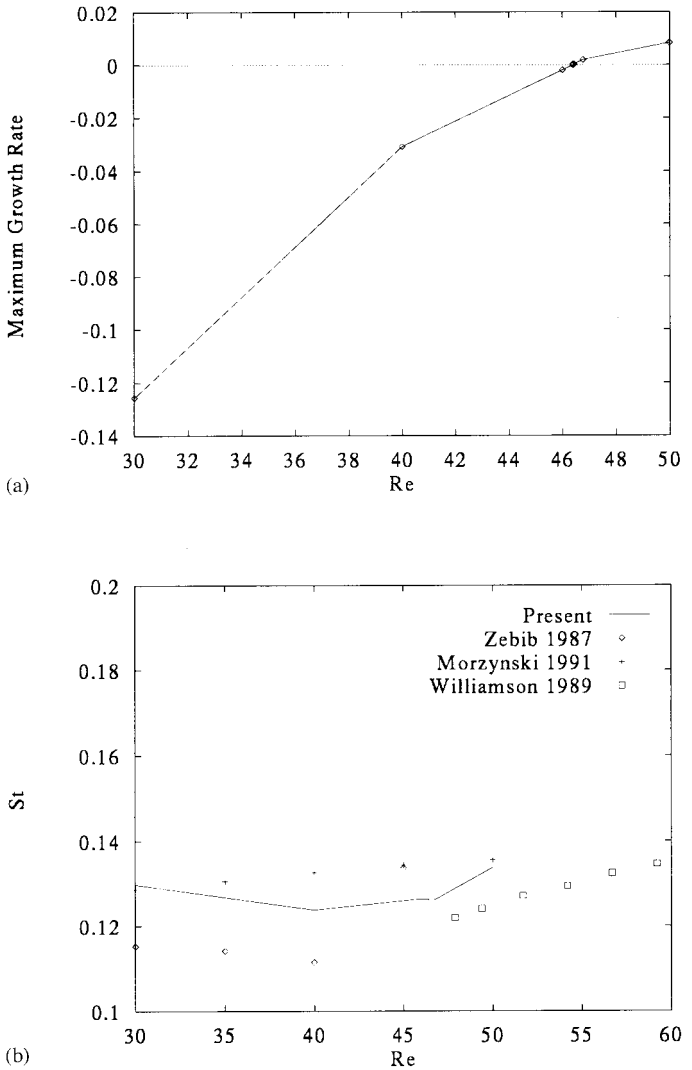

Figure 14. The maximum growth rate and the Strouhal number for the circular cylinder flow. (a) Maximum growth rate vs. *Re*; (b) Strouhal number vs. *Re*.

Table V. Convergence of the leading eigenvalue in the circular cylinder flow for Re_c

No.	ω_r	St_c	ε	m
1	2.8050270D-04	1.2518878D-01	5.8726178D-05	60
2	2.7990421D-04	1.2618908D-01	1.4998004D-11	100
3	2.7990421D-04	1.2618909D-01	7.1128622D-16	150

of the St_c with experimental data [3] and other results from two-dimensional instability analysis [10,37] is shown in Figure 14(b). The present St_c is close to the averaged value of those results.

In order to search for a self-organized structure in the onset of the primary instability, the vectors for the eigenfunction of $\hat{u}$ and $\hat{v}$ are plotted in Figure 15(a) for the real part and in (b) for the imaginary part. It shows, apparently, that the instability of the external flow, such as the flow past a circular cylinder, belongs to the *convective instability* class [2], since the

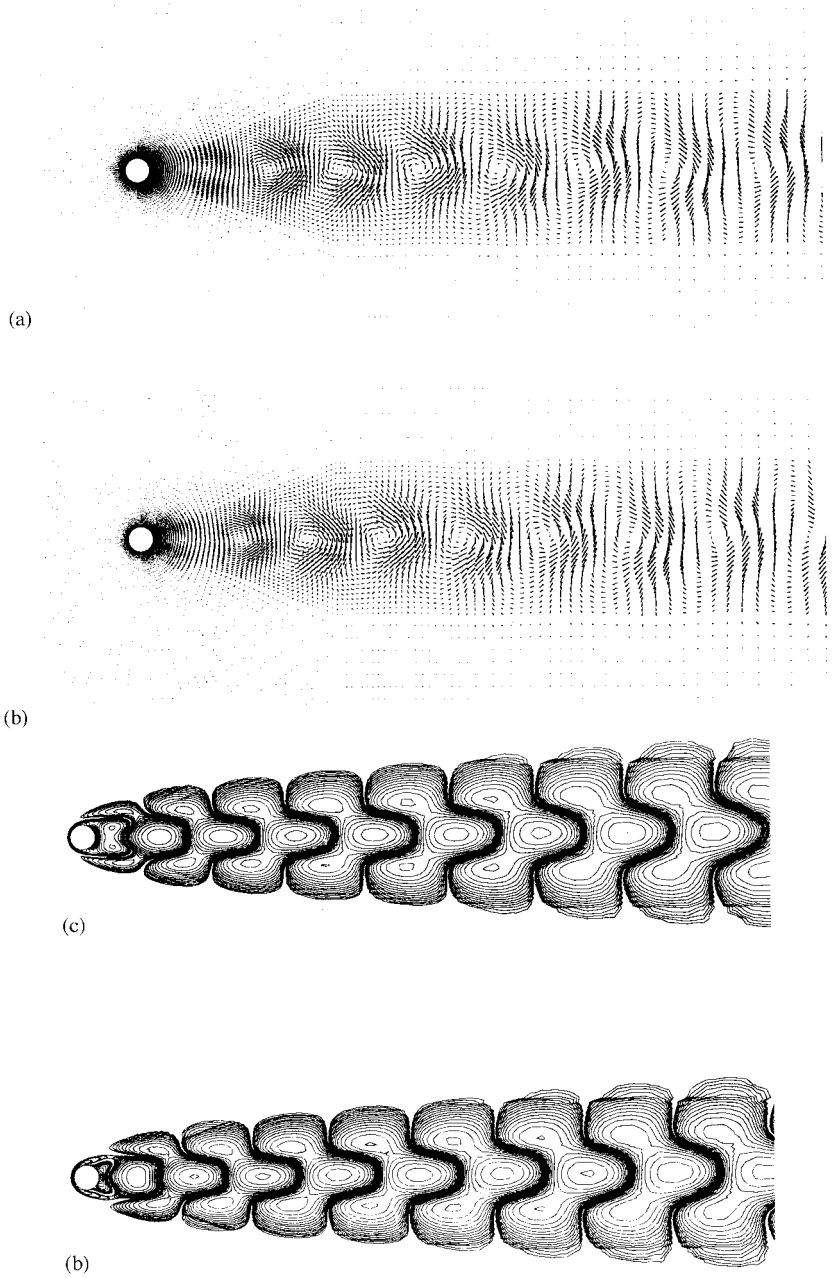

Figure 15. Eigenfunctions of velocities and perturbed normal vorticities. (a) Real part of eigenfunction; (b) imaginary part of eigenfunction; (c) perturbed vorticity $\hat{\omega}_{z\mathrm{r}}$; (d) Perturbed vorticity $\hat{\omega}_{z\mathrm{i}}$.

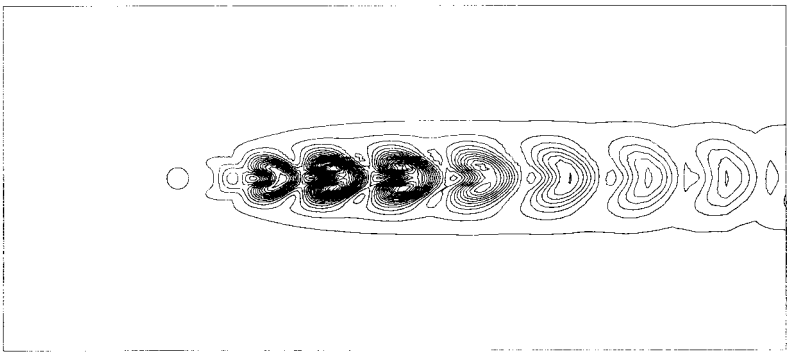

(a)

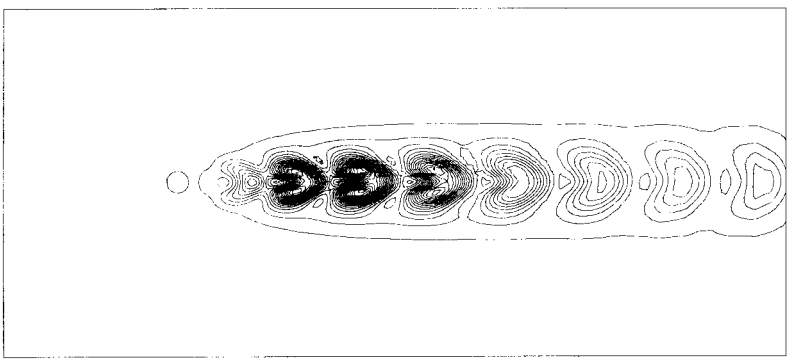

(b)

Figure 16. Distribution of the energy e for $Re = 50$ at (a) $t = 0.0$ and (b) $t = T/2$.

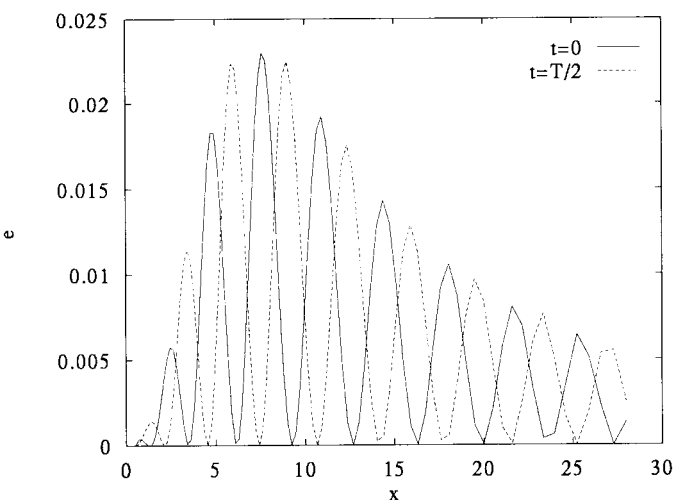

Figure 17. Energy variation on the rear centreline of the flow for $Re = 50$.

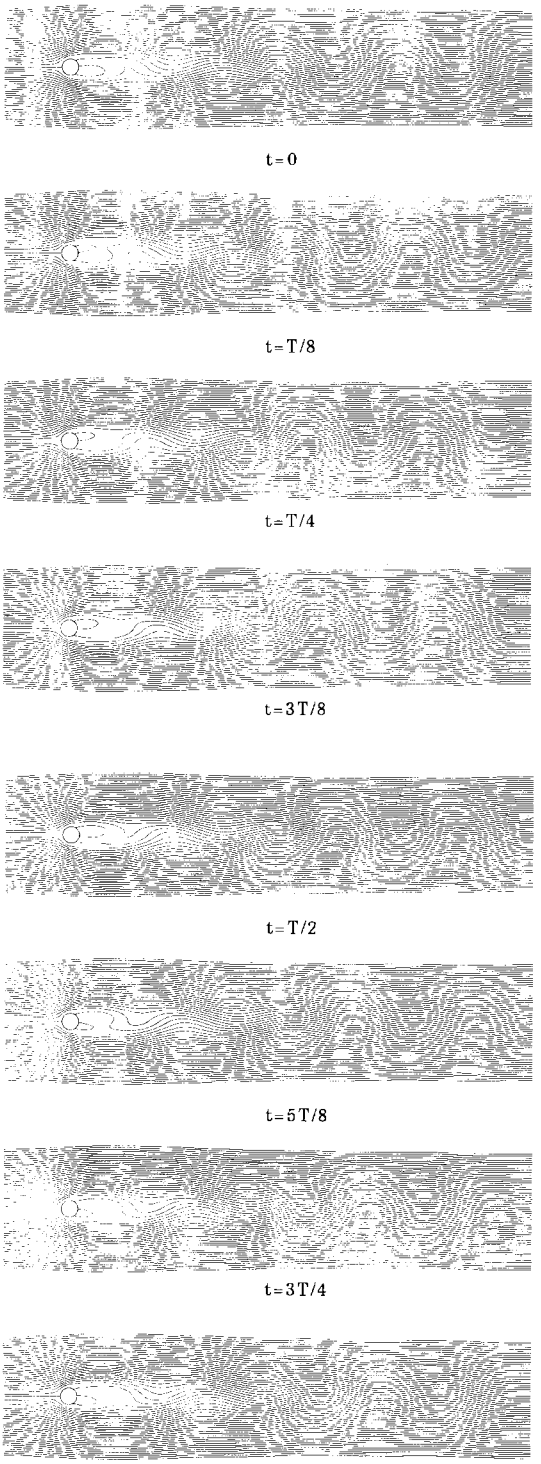

(a)

Figure 18. Snapshots of the instantaneous streamline and normal vorticity ω_z, at intervals of $\frac{1}{8}$ the period of oscillation, for a flow at Re slightly greater than Re_c. (a) Instantaneous streamlines; (b) vorticity ω_z.

t=0

t=T/8

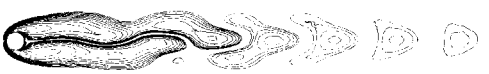

t=T/4

t=3T/8

t=T/2

t=5T/8

t=3T/4

(b) t=7T/8

Figure 18 (*Continued*)

amplitude of the velocity increases along the streamwise direction. Further, a perturbation of the normal vorticity ω'_z is defined as

$$\omega'_z = \omega_z - \Omega_z, \tag{37}$$

where Ω_z denotes the normal vorticity of steady state, then

$$\omega'_z = i\frac{1}{2}\left(\frac{\partial \hat{v}}{\partial x} - \frac{\partial \hat{u}}{\partial y}\right)\exp(\omega t) = (-\hat{\omega}_{zi} + i\hat{\omega}_{zr})\exp(\omega t). \tag{38}$$

The perturbed vorticities $\hat{\omega}_{zr}$ and $\hat{\omega}_{zi}$ are depicted in Figure 15(c) and (d), where the saddle-like vorticity distribution is bifurcated in the streamwise direction. Moreover, the perturbed vortices are shed alternatively behind the circular cylinder, and the sign of the saddle-like vorticity is also changed alternately in Figure 15(c) and (d). From these figures, because of the existence of symmetry in the perturbation part of the wake past the circular cylinder, its destabilization in the primary transition of cylinder flow will lead to the onset of the von Kármán vortex street. Then, the *intrinsically* self-organized structure of vortex shedding will occur.

The instability of flow past a circular cylinder belongs to the *convective instability* class as discussed in the review of Hurre and Monkewitz [2]. To understand the mechanism of instability, the spatio-temporal variation of the disturbance energy e (i.e. turbulence energy) for the wake of the circular cylinder flow at Re slightly greater than the Re_c obtained above is investigated. This energy is defined as

$$e = \frac{1}{2}(u'^2 + v'^2 + w'^2). \tag{39}$$

The spatio-temporal variations of the energy e for $Re = 50$ at time $t = 0.0$ and $T/2$ are plotted in Figure 16(a) and (b). These figures show that the high energy area is limited within the wake of the flow, and transmitted downstream. In addition, the spatial distribution of the energy is symmetric in the wake for low Reynolds number. Further, the energy variations on the rear centreline of the flow for $Re = 50$ are depicted in Figure 17. The energy increases over the distance $x = 0.5 \sim 10L$, and decays from the distance $x = 10L$, where L is the diameter of the circular cylinder. At the same time, the disturbance is travelling downstream. This phenomenon has been expressed as *convective instability* [2].

4.2.3. Reconstruction of vortex shedding for critical flow. The superposition of spectra for $Re = 50$, as described in (42) and (43), is used to reconstruct the vortex shedding. Figure 18 shows a sequence at intervals of $\frac{1}{8}$ of a period of oscillation of 'snapshots' of the instantaneous streamfunction in (a) and the normal vorticity ω_z in (b) derived from the velocities u and v. This figures reproduces completely the vortex shedding for supercritical flow, such as the $Re = 50$.

5. CONCLUSIONS

In this study, the linear stability of incompressible fluid flows in lid-driven cavity and past a circular cylinder were investigated by using the mixed finite element method under the assumption of slight compressibility forced in the Navier–Stokes equations. From the obtained results, the conclusions are as follows:

(1) By means of the P_2P_1 triangular element, the spatial oscillation of pressure is avoidable. Moreover, the difference of stability results from P_2P_1 and P_1P_1 elements is negligible. Therefore, for the stability analysis of incompressible flow, the mixed finite element is numerically more elegant.

(2) It is reasonable to use compressibility based on physical meaning to reduce the singularity in the generalized eigenproblem that occurs in the linear stability of incompressible fluid flow.

(3) Arnoldi's method with linear fractional transformation is very effective to detect the dominant parts of eigenvalues. In addition, the difficulty of ill-conditioned eigenproblems can be overcome effectively, while maintaining higher accuracy of the eigenvector.

For the instability analysis of lid-driven cavity flow, our conclusions are:

(4) The estimated critical results in the case are 920.277 ± 0.010 for the Reynolds number and 7.40 ± 0.02 for the wave number in which the non-dimensional frequency is 0.0788. These results are in agreement with the observation of Aidun *et al.* [1] and are more accurate than those of finite difference. This instability in the cavity is associated with *absolute instability* [2].

(5) Through the reconstruction of flows in the critical mode, the three-dimensionality in cavity flow is apparent. By means of investigation of the instability mechanism, these results show that the TGL vortices play a key role in generating three-dimensional flow patterns in the cavity.

For the primary instability analysis of flow past a circular cylinder, the conclusions are:

(6) The accurate critical values of primary instability are $Re_c = 46.389 \pm 0.010$ and $St_c = 0.126$. These values are very close to the observation data [3] and other stability results [10,13].

(7) It is verified that the primary onset of the Kármán vortex street is two-dimensional. The primary instability at the Hopf bifurcation point is connected with the symmetry-breaking bifurcation of spectra. The further study about the three-dimensionality of the secondary instability over $Re = 150 \sim 200$ using the FEM can be referred to [38].

(8) By means of the discussion of the spatio-temporal variation of the disturbance energy for the supercritical flow, the existence of the *convective instability* in external flows, such as circular cylinder flow, is verified.

Finally, based on the efficiency of this analysis method and the incorporation of physical compressibility in the disturbance equations in these cases, the present method can also be used for the stability analysis of compressible fluid flows.

REFERENCES

1. C.K. Aidun, N.G. Triantafillopoulos and J.D. Benson, 'Global stability of lid-driven cavity with throughflow: flow visualization studies', *Phys. Fluids*, **A3**, 2081–2091 (1991).
2. P. Huerre and P.A. Monkewitz, 'Local and global instabilities in spatially developing flows', *Annu. Rev. Fluid Mech.*, **22**, 473–537 (1990).
3. C.H.K. Williamson, 'Oblique and parallel modes of vortex shedding in the wake of a circular cylinder at low Reynolds numbers', *J. Fluid Mech.*, **206**, 579–627 (1989).
4. N. Ramanan and G. M. Homsy, 'Linear stability of lid-driven cavity flow', *Phys. Fluids*, **6**, 2690–2701 (1994).
5. S.A. Orszag, 'Accurate solution of the Orr–Sommerfelt', *J. Fluid Mech.*, **50**, 689–703 (1971).
6. L. Kleiser and T.A. Zang, 'Numerical simulation of transition in wall-bounded shear flows', *Annu. Rev. Fluid Mech.*, **3**, 495–537 (1991).
7. M.R. Malik and D.I.A. Poll, 'Effect of curvature on three-dimensional boundary-layer stability', *AIAA J.*, **23**, 1362–1369 (1985).
8. M.R. Khorrami, M.R. Malik and R.L. Ash, 'Application of spectral collocation techniques to the stability of swirling flows', *J. Comp. Phys.*, **81**, 206–229 (1989).
9. M.R. Malik, 'Numerical methods for hypersonic boundary layer stability', *J. Comput. Phys.*, **86**, 376–413 (1990).
10. M. Morzynski and F. Thiele, 'Numerical stability analysis of a flow about a cylinder', *Z. Angew. Math. Mech.*, **71**, T424–T428 (1991).

11. M. Morzynski, 'Numerical investigation of wake instability', in H. Eckelmann *et al.* (eds.), *Bluff-Body Wakes, Dynamics and Instabilities*, *IUTAM Symposium*, *Gottingen*, *Germany*, Springer, Berlin, 1992.
12. Y.S. Li and S.C. Kot, 'One-dimensional finite element method in hydrodynamic stability', *Int. J. Numer. Methods Eng.*, **17**, 853–870 (1981).
13. C.P. Jackson, 'A finite-element study of the onset of vortex shedding in low past variously shaped bodies', *J. Fluid Mech.*, **182**, 23–45 (1987).
14. M. Kawahara and Y. King, 'Bifurcation analysis of brown tide by reaction–diffusion equation using finite element method', *J. Comp. Phys.*, **131**, 253–266 (1997).
15. D.S. Malkus, 'Eigenproblems associated with the discrete LBB conditions for incompressible finite elements', *Int. J. Eng. Sci.*, **19**, 1299–1310 (1981).
16. M.D. Gunzburger, 'Navier–Stokes equations for incompressible flows: finite element methods', in Roger Peyret (ed.), *Handbook of Computational Fluid Mechanics*, Academic Press, New York, 1996, p. 106.
17. Y. Ding and M. Kawahara, 'Linear stability of incompressible flow using a mixed finite element method', *J. Comp. Phys.*, **139**, 243–273 (1997).
18. C.H.K. Williamson, 'Vortex dynamics in the cylinder wake', *Annu. Rev. Fluid. Mech.*, **28**, 477–539 (1996).
19. Y. Ding and M. Kawahara, 'Improved velocity correction method with constraint of continuity using finite element method', *Comput. Struct.*, 1997, submitted.
20. Y. Ding and M. Kawahara, 'Linear stability of incompressible fluid flow using finite element method', in H. Kubota (ed.), *Second Asia Workshop on CFD*, 1996, pp. 55–60.
21. J. Kim and P. Moin, 'Application of a fractional-step method to incompressible Navier–Stokes equations', *J. Comp. Phys.*, **59**, 308–232 (1985).
22. R. Kessler, 'Non-linear transition in three-dimensional convection', *J. Fluid Mech.*, **174**, 357–379 (1987).
23. Z.U.A. Warsi, *Fluid Dynamics—Theoretical and Computational Approaches*, CRC Press, FL, 1993, p. 45.
24. C.B. Jiang and M. Kawahara, 'A three-step finite method for unsteady incompressible flows', *Comput. Mech.*, **11**, 355–370 (1993).
25. D.M. Hawken, H.R. Tamoddon-Jahromi, P. Townsend and M.F. Webster, 'A Taylor–Galerkin-based algorithm for viscous incompressible flow', *Int. J. Numer. Method Fluids*, **10**, 327–351 (1990).
26. Y. Saad, 'Variation on Arnoldi's method for computing eigenelements of large unsymmetric matrices', *Linear Algebra Appl.*, **34**, 269–295 (1980).
27. W.E. Arnoldi, 'The principle of minimized iterations in the solution of the matrix eigenvalues problem', *Q. Appl. Math.*, **9**, 17–29 (1951).
28. N. Nayar and J.M. Ortega, 'Computation of selected eigenvalues of generalized eigenvalue problems', *J. Comput. Phys.*, **108**, 8–14 (1993).
29. H.C. Elman, 'A stability analysis of incomplete LU factorization', *Math. Comput.*, **47**, 191–217 (1986).
30. H.C. Elman, 'Relaxed and stabilized incomplete factorizations for non-self-adjoint linear systems', *BIT*, **29**, 890–915 (1989).
31. Y. Ding and M. Kawahara, 'Linear stability of incompressible fluid flow in cavity using finite element methods', *Int. J. Numer. Methods Fluids*, **27**, 139–157 (1998).
32. W.J. Stewart and A. Jennings, 'A simultaneous iteration algorithm for real matrices', *ACM Trans. Math. Software*, **7**, 184–198 (1981).
33. Y. Huang, U. Ghia, G.A. Osswald and K.N. Ghia, 'Velocity–vorticity simulation of unsteady 3D viscous flow within a driven cavity', in M. Deville, T.-H. Le and Y. Morchoisne (eds.), *Numerical Simulation of 3D Incompressible Unsteady Viscous Laminar Flows (Notes on Numerical Fluid Mechanics, 36)*, Vieweg Press, Wiesbaden, 1992, pp. 54–66.
34. L. Janvier, B. Metivet, R. Mgouni, G. Pot and E. Razafindrakoto, 'A 3D driven cavity flow simulation with N3S code', in M. Deville *et al.* (eds.), *Numerical Simulation of 3D Incompressible Unsteady Viscous Laminar Flows (Notes on Numerical Fluid Mechanics, 36)*, Vieweg Press, Wiesbaden, 1992, pp. 67–78.
35. E. Berger and R. Wille, 'Periodic flow phenomena', *Annu. Rev. Fluid Mech.*, **4**, 313 (1972).
36. P.M. Gresho, S.T. Chan, R.L. Lee and C.D. Upson, 'A modified finite element method for solving the time-dependent incompressible Navier–Stokes equations. Part 2 Applications', *Int. J. Numer. Methods Fluids*, **4**, 619 (1984).
37. A. Zebib, 'Stability of viscous flow past a circular cylinder', *J. Eng. Math.*, **21**, 155–165 (1987).
38. Y. Ding and M. Kawahara, 'Secondary instabilities of wakes of a circular cylinder using finite element method', *Int. J. Comput. Fluid Dyn.* (1998) submitted.

